Honeycomb Structures of Bulk Metallic Glasses

*Baran Sarac, Jittisa Ketkaew, Dawn Olivia Popnoe, and Jan Schroers**

A combination of lithography and thermoplastic forming allows us to fabricate honeycombs from bulk metallic glass (BMG) precisely and to manipulate its structure selectively. Characteristics of the honeycomb such as the ligament length, thickness, and radius of curvature at the joints of the cells are varied to determine how changes in these characteristics affect properties under uniaxial in-plane compression testing. It is found that the deformation behavior of BMG honeycombs can be controlled through microstructural design, from brittle to ductile, by changing the length to thickness ratio of the ligaments. The ability to absorb energy of BMG honeycombs exceeds honeycombs of most other materials due to the utilization of a size effect, which result in plasticity. Besides the usage for BMG honeycombs, the technique provides a general method to effectively characterize complex microstructural architectures and tailoring these architectures to the specifications of the material used.

1. Introduction

Bulk metallic glasses have received a lot of attention in the last two decades for their high strength and elasticity which are consequences of their amorphous structure and concomitant lack of dislocations and associated slip planes.[1] Upon yielding, however, BMGs suffer from a strong tendency toward shear localization, which results in macroscopically brittle failure at ambient temperatures.[2] The lack of macroscopic plasticity is considered the Achilles' heel of BMGs and has prevented widespread proliferation of BMGs as a structural material. However, when BMGs are used in geometries where one dimension is below about 10 times its critical crack length (~1 mm for a medium range Zr-based BMG), they exhibit significant bending plasticity.[3] This feature, and other size effects have been widely explored in foams to design overall plasticity.[4–10] In addition to the potential for microstructural architecture design, the unusual high ratio of yield strength over modulus of BMGs suggests that a transition from plastic yielding to elastic buckling can be realized for practical l/t ratios (l: ligament length, t: ligament thickness). Systematic studies of such effects have been difficult since fabrication methods for stochastic foams[10,11] and microstructural architecture designed by perforation-stretching[12,13] provide limited control over microstructural features, especially when independent manipulation of features is desired.

Here, we present a method that allows varying individual microstructural features independently with unprecedented versatility and accuracy. To fabricate BMG honeycombs, we utilize thermoplastic forming (TPF) of BMGs[14–17] using molds that are produced through photolithography. Regular honeycomb structures ($\theta = 30°$ and $h = l$) are used as a case study since they are widely studied. BMGs are suitable to be used in such structures, and mathematical models have been developed.[11,18–24] To cover the range of elastic buckling and plastic yielding, a broad spectrum of honeycomb ligament length to thickness ratio has been evaluated. Furthermore, corner-fillets are used as a design tool to dissipate energy more homogenously throughout the BMG honeycombs. Here, two metallic glasses with different characteristics are presented. Their performances in honeycomb structures are compared to conventional metals (superplastic aluminum alloy (2004Al), Zn) and plastics (polyether ether ketone (PEEK), polyethylene (PE)). To even extend the range of materials, we also utilized crystallization and structural relaxation of the BMGs, which drastically changes their mechanical behavior.

2. Results and Discussion

We consider $Zr_{35}Ti_{30}Cu_{7.5}Be_{27.5}$ as a typical BMG with negligible macroscopic plasticity[25] and, as a comparison, $Pt_{57.5}Cu_{14.7}Ni_{5.3}P_{22.5}$, which exhibits unusually high, ~20% compressive plasticity.[26] Both alloys are well suited for the TPF fabrication of the honeycomb due to their high formability.[27] **Figure 1** shows the fabrication steps of BMG honeycombs. As the first step, molds for BMG honeycombs were designed using a CAD program, which were subsequently patterned onto a photomask through direct laser beam writing. The photomask was then transferred onto a Si wafer by UV exposure of the

B. Sarac, Prof. J. Schroers
Department of Mechanical Engineering & Materials Science Yale University
15 Prospect St BCT RM 216-217
New Haven, CT 06511 USA
E-mail: jan.schroers@yale.edu
J. Ketkaew
Department of Chemistry
Faculty of Science
Chulalongkorn University
Phayathai Road, Patumwan Bangkok 10330, Thailand
D. O. Popnoe
Department of Physics
Angelo State University
2601 W.Avenue N, San Angelo, TX, 76909, USA

DOI: 10.1002/adfm.201200539

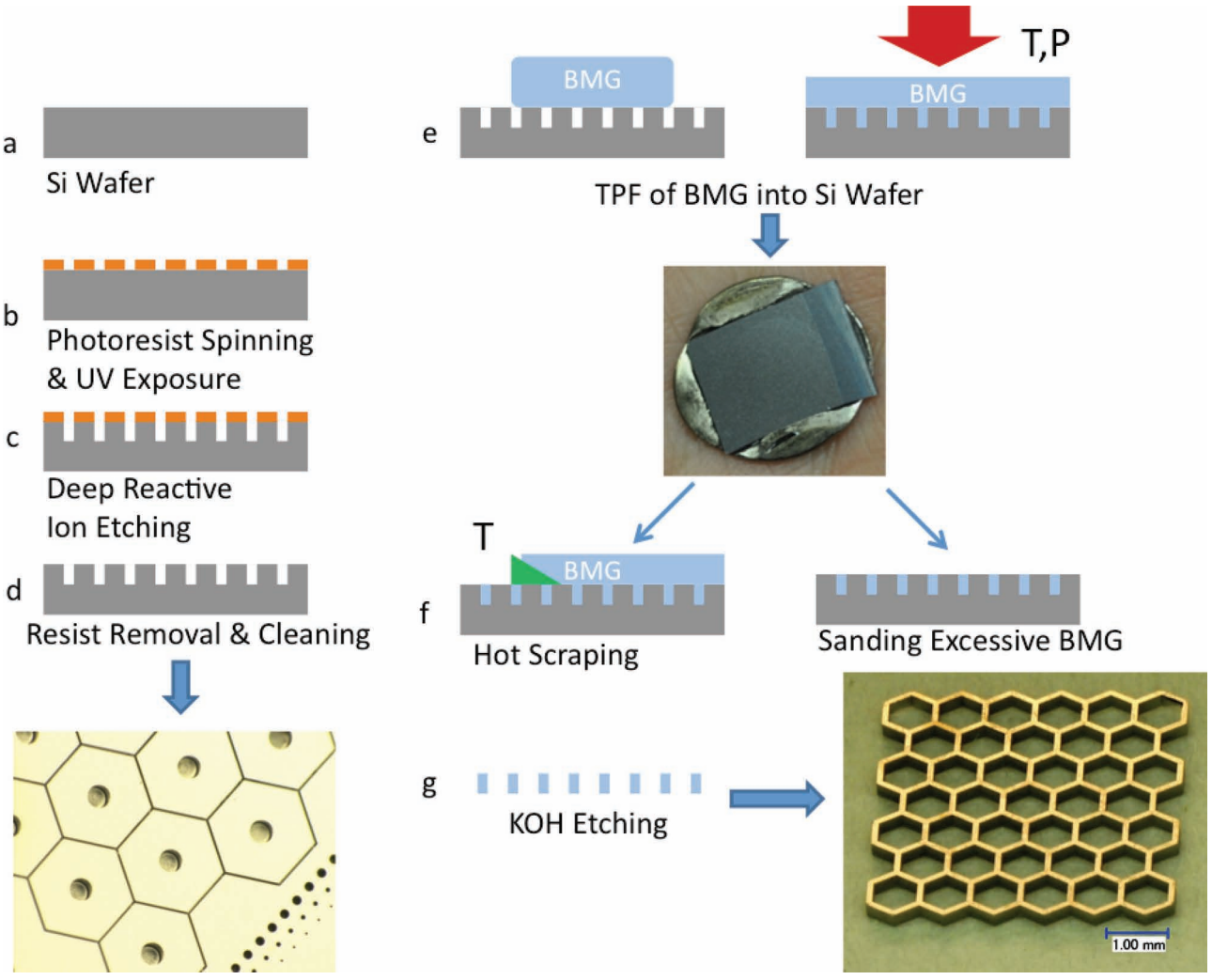

Figure 1. Schematics of the BMG honeycomb fabrication. a) Silicon is used as a mold material. b) A thin layer of photoresist on the Si wafer is patterned by UV exposure through a mask. c) The exposed regions of the Si wafer are etched by deep reactive ion etching (DRIE). d) The residual photoresist is removed. e) The etched Si wafer, containing the honeycomb features, is filled with Zr- or Pt-BMG by TPF based compression molding. f) Residual BMG is either removed by hot scraping or polishing. g) The honeycomb of 39 cells is released by etching the Si wafer in KOH.

photoresist. The etching depth of the honeycomb molds was controlled through the etching time. The BMG honeycombs were produced by thermoplastic pressing of $Zr_{35}Ti_{30}Cu_{7.5}Be_{27.5}$ at 425 °C and 275 °C for $Pt_{57.5}Cu_{14.7}Ni_{5.3}P_{22.5}$ in air into the honeycomb mold for 60 s under a pressure of 50 MPa. The extra BMG layer was removed by either hot cutting[14] at 390 °C or by polishing. The BMG honeycomb comprised of 39 cells was subsequently released from the mold by etching the Si mold in KOH for 30 min at 100 °C. The amorphous structure of the BMG honeycomb was confirmed by thermal analysis using differential scanning calorimetry. Even though unsuited for large-scale commercial manufacturing, this fabrication method enables a very precise, highly versatile, and high-throughput test sample fabrication. Typically, approximately 200 silicon molds can be fabricated simultaneously at a precision of better than one micron in the lateral dimensions (**Figure 2**). This precision is translated into the BMG honeycomb through TPF,[28] where the only measurable discrepancy between the BMG honeycombs and the Si mold is due to the difference in the thermal expansion coefficients ($\alpha_{BMG} \sim 4 \times 10^{-5}$/ °C,[29] $\alpha_{Si} = 3.7 \times 10^{-6}$/ °C). To demonstrate the precision, Figure 2c depicts both the feature, which was drawn in the mask, and its realization in the BMG through TPF. Our setup to characterize the honeycomb structures under quasi-static compression conditions is shown in **Figure 3**. Load cells with a maximum load of 10 N, 100 N and 1000 N were selected depending on the l/t ratio of the honeycomb. Custom made pneumatic grips with grids were used to prevent slippage and guarantee precise alignment. Our setup allows us to record simultaneously stress-strain diagrams and visualize the deformation, hence, to correlate microstructural events with the stress-strain diagram. To prevent out-of-plane buckling, the depth of the honeycomb (out-of-plane) must result in a moment of inertia such that in-plane yielding occurs at a lower stress level than out-of-plane buckling. Thus, $F_{cr} = \frac{E I \pi^2}{A L^2} > \sigma_y$ with E: Young's modulus of the bulk BMG, I: moment of inertia, L: height of the

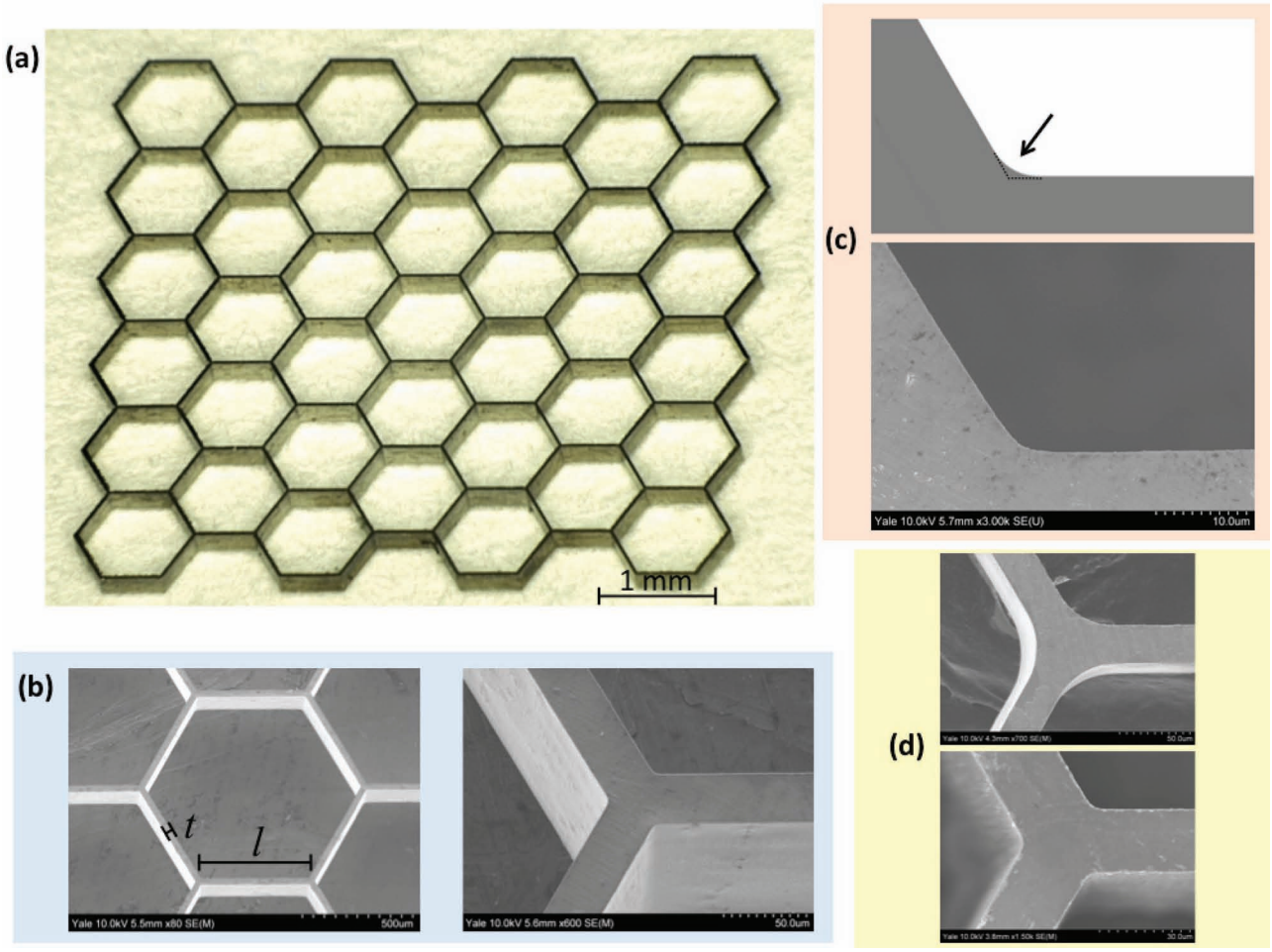

Figure 2. a) Zr-BMG honeycomb with $l/t = 20$ and a depth of 200 µm. b) Close-up image of a honeycomb cell, and its joint. c) Corner-fillets to reduce stress concentrations in the honeycomb's joints. The top image shows the drawing, and the bottom image the realization in the actual BMG honeycomb, which demonstrates our control of better than 1 µm dimensional accuracy. d) Corner-fillets of $r = 50$ µm (top), $r = 6$ µm (bottom).

honeycomb, A: cross-sectional area of the honeycomb, F_{cr}: critical buckling stress, and σ_y: yield strength of the bulk BMG.

While the out-of-plane buckling must be prevented through proper design of the sample for accurate experiments, in plane buckling is explored as a design tool. In-plane elastic buckling occurs due to an Euler buckling instability for l/t values exceeding a critical ratio. This critical ratio can be correlated to the material's properties, namely E/σ_y, through:[30]

$$\left(\frac{\rho_s}{\rho^*}\right)_{\text{crit}} = \frac{\sqrt{3}}{2}\left(\frac{l}{t}\right)_{\text{crit}} = \frac{1}{2\sqrt{3}}\left(\frac{E}{\sigma_y}\right)_{\text{bulk}} \quad (1)$$

where ρ_s denotes the bulk density and ρ^*, the density of the honeycomb. Elastic buckling occurs for structures with $l/t > [l/t]_{crit}$. For example, superplastic aluminum alloy (2004Al) requires $[l/t]_{\text{crit}} \cong 82$ ($E = 74$ GPa, $\sigma_y = 300$MPa),[31] which corresponds to a low honeycomb density of $\rho^*/\rho_s = 1.4\%$, preventing elastic buckling when used in practically realizable honeycomb structures. On the other hand, elastic buckling can readily be realized in plastics, such as low density polyethylene ($E = 0.4$ GPa, $\sigma_y \cong 15$ MPa),[32] which leads to $[l/t]_{\text{crit}} = 15.0$ and $\rho^*/\rho_s = 13.0\%$. For BMGs, the relatively low E/σ ratio, e.g., $Zr_{35}Ti_{30}Cu_{7.5}Be_{27.5}$ ($E = 87$ GPa, $\sigma_y = 1430$ MPa),[25] results in $[l/t]_{\text{crit}} = 20.4$ and $\rho^*/\rho_s = 5.7\%$. This density can be readily achieved in BMG honeycomb structures. The significantly higher strength of BMGs compared to plastics suggests that yielding and buckling of BMGs occurs at a stress level, which are approximately two orders of magnitude higher than yielding and buckling of plastics.

Figure 4 shows quasi-static compression of a Zr-BMG honeycomb ($l = 500$ µm, $t = 10$ µm, $l/t = 50 > l/t_{\text{crit}} = 20.4$) at a strain rate of 0.005 mm/s. The stress-strain curve of the in-plane compression shows a linear-elastic region (Figure 4a-1). In order to determine the non-linear elastic deformation, additional experiments of cyclic loading to a progressively higher strain reveal 25% elastic strain. Up to the first stress drop, the so-called stress initiation σ_I, (Figure 4a-2), the deformation appears homogenously distributed throughout the structure. However, it can already be anticipated where strain localization will occur (Figure 4a-3). Upon further deformation, the strength decreases due to an instability of the ligaments, causing the strain to localize in the bottom row of the honeycomb structure (Figure 4a-4, 5). Such instabilities, which cause strain localization and result in stress fluctuations, are designated by seven stress hills and valleys in the stress–strain diagram.

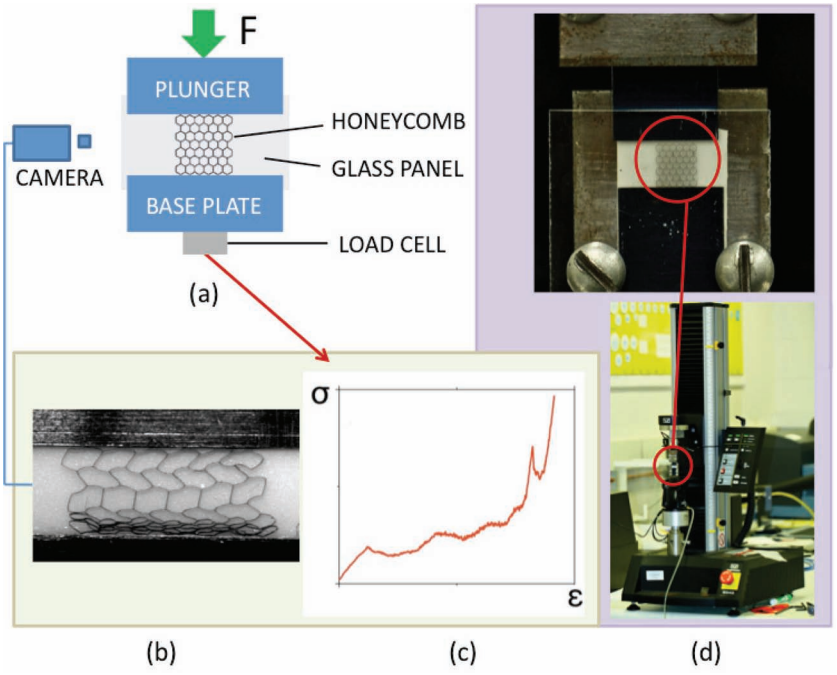

Figure 3. Experimental setup for quasi-static characterization of honeycomb test samples. a) Schematic of the mold used in this study. The honeycomb rests on a base plate, which is positioned between the metal mold and the transparent glass panel with a clearance exceeding the depth of the honeycomb. In-plane deformation of a honeycomb is achieved by pressing a flat steel plate with a constant strain rate of 0.005 mm/s. b) *In-situ* visualization of the deforming BMG honeycomb. c) Stress-strain diagram generated by the output signal of the load cell. d) Actual experimental setup for quasi-static characterization to show the honeycomb sample positioned inside the Instron Testing machine.

Figure 4b shows the in-plane compressive deformation of $Zr_{35}Ti_{30}Cu_{7.5}Be_{27.5}$ honeycomb with $l/t = 5 < [l/t]_{crit}$. This honeycomb exhibits significantly different properties than the $l/t = 50$ honeycomb. For $l/t = 5$, deformation is highly localized and forms a ~45° angle with the loading direction, typical for the yielding of bulk BMGs under compression.[33,34] Plastic strain is highly localized within a narrow band - similar to the formation of shear bands in bulk metallic glasses - which results in pronounced stress drops owing to fracture of the honeycomb cells. In contrast, for the honeycombs with $l/t > l/t_{crit}$, yielding occurs in a plane parallel to the loading direction, which is typical for ductile materials. The microscopic mechanism for plastic deformation under in-plane compression of BMG honeycombs changes with l/t. For honeycombs with $l/t < l/tl/t_{crit}$, deformation occurs through ligament fracture in the highly localized regions, whereas for $l/tl/t > l/tl/t_{crit}$ honeycombs deform plastically without breakage all the way up to densification (ε_D). Not only do these two honeycomb types differ in the deformation mode, but they also show remarkable differences in their initiation stress (σ_l), and elasticity (ε_{el}).

Figure 5 exhibits the stress–strain curves for $Zr_{35}Ti_{30}Cu_{7.5}Be_{27.5}$ honeycombs with various l/t ratios under uniaxial in-plane compression. When l/t decreases from 50 to 2.5, the honeycomb's strength increases by two orders of magnitude; ~1 MPa for $l/t = 50$ ($\rho^*/\rho_s = 2.3\%$) up to 300 MPa for $l/t = 2.5$ ($\rho^*/\rho_s = 41.0\%$), indicating a nonlinear relationship with density.

To compare BMG honeycombs with other materials, polyether ether ketone (PEEK) and polyethylene (PE) were chosen as representatives for plastics, and 2004Al and zinc as representatives for crystalline metals. One main criterion for the selection of these representative materials is their suitability for our fabrication process (Figure 1).

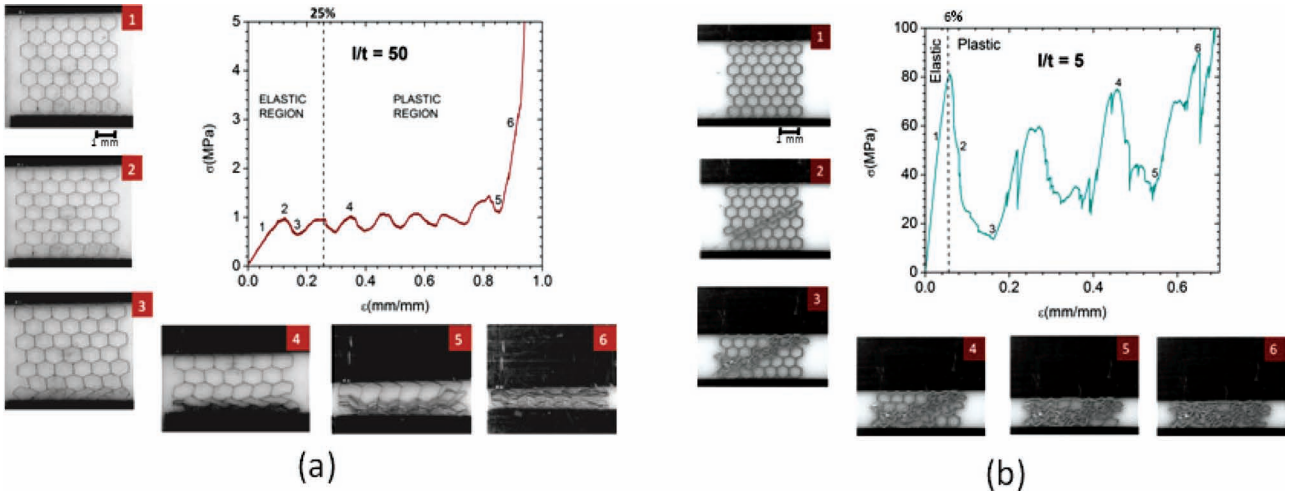

Figure 4. Stress-strain diagram of in-plane compression of $Zr_{35}Ti_{30}Cu_{7.5}Be_{27.5}$ honeycomb (a) $l/t = 50$ ($t = 10$ μm). The honeycomb exhibits in-plane elastic bending strain of 25%, which further deforms plastically until ε_D without ligament fracture. Panels (1–6) show the microstructural events correlated with the stress-strain curve. b) $l/t = 5$ ($t = 100$ μm). This honeycomb shows an overall elastic strain of 6%, and beyond this point, exhibits a brittle deformation behavior with a localized deformation forming a ~45 ° angle with the load direction. Stress fluctuation values ($\Delta\sigma_a$) increases with l/t decreasing because the amount of stress to create instability at the cell ligaments increases. However, σ_a normalized by the initiation strength of the same honeycomb (σ_l) is found to be independent of the l/t ratio of the honeycomb.

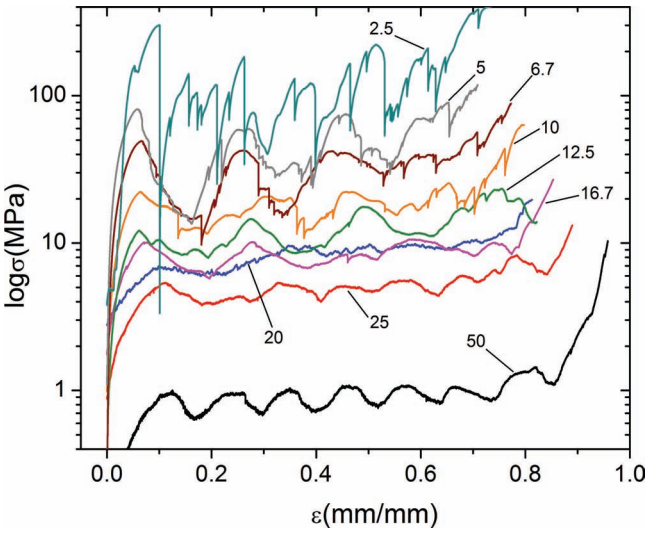

Figure 5. Stress-strain curve for $Zr_{35}Ti_{30}Cu_{7.5}Be_{27.5}$ honeycombs with varying l/t. Numbers indicate their l/t ratio. Strength of the honeycomb increases by two orders of magnitude with l/t decreasing from 50 to 2.5.

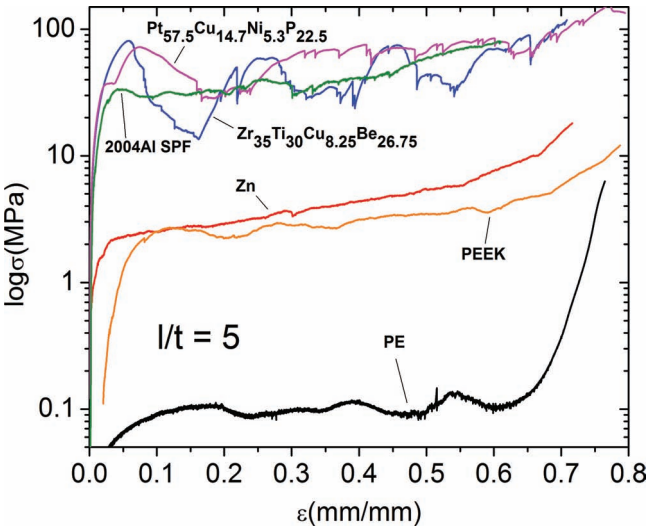

Figure 6. Stress-strain curves of honeycombs with l/t = 5, covering four orders of magnitude fabricated from $Zr_{35}Ti_{30}Cu_{7.5}Be_{27.5}$, $Pt_{57.5}Cu_{14.7}Ni_{5.3}P_{22.5}$, 2004Al, zinc, polyether ether ketone (PEEK), and polyethylene (PE). Note that the control honeycombs are made of much lighter materials (except Zn), which partially explains their lower mechanical properties.

PEEK and PE were formed below its melting temperature at 340 °C ($T_{m\ (PEEK)}$ = 343 °C) and at 110 °C ($T_{m\ (PE)}$ = 120 °C) under a pressure of 10 MPa, respectively. Similarly, 2004Al and Zn were formed at 500 °C ($T_{process\ (2004Al)}$ = 460 °C) and 410 °C ($T_{m\ (Zn)}$ = 420 °C) under 30 MPa pressure, respectively. Their behavior under quasi-static loading is shown in **Figure 6**. The initiation strength of $Zr_{35}Ti_{30}Cu_{7.5}Be_{27.5}$ honeycomb exceeds those of other considered materials; it is almost three orders of magnitude higher than for PE, around thirty times higher than for PEEK, and three times higher than that for 2004Al honeycomb. When normalized by density, the difference in initiation strength between Zr-BMG and 2004Al is still two times (**Table 1**).

Figure 7a shows the energy absorption per unit volume (W) until densification ε_D for different l/t ratios of $Zr_{35}Ti_{30}Cu_{7.5}Be_{27.5}$ honeycombs calculated through $W = \int_0^{\varepsilon_D} \sigma d\varepsilon$. With decreasing l/t, the absorbed energy increases rapidly. The honeycomb with l/t = 2.5 absorbs almost five times the energy than bulk Zr-BMG. This suggests that porosity can be used as an effective design tool to enhance energy absorption mechanism for metallic glasses. For example, W of a honeycomb with l/t = 10 (ρ^*/ρ_s = 11.2%) is comparable to that of the bulk BMG, however, at only 10% of its weight (Figure 7a inset). Compared to other BMG cellular structures, the energy absorption measured here for the BMG honeycomb represents the upper bound (Figure 7b).[10,35–37] Compared to the other materials considered here, the BMG honeycomb (l/t = 5) absorbs approximately one order of magnitude more energy than PEEK, Zn, and PE, and approximately twice that of 2004Al. When energy absorption is normalized by density, BMG and 2004Al honeycombs are comparable.

As a design tool to enhance BMG honeycomb performance, we considered honeycomb cell corner-fillets to reduce stress concentrations (see Figure 2e). To study the effectiveness of filleting, we used cell joints of different radii in a l/t = 25

Table 1. Mechanical properties of honeycombs from different materials. Errors are on the order of the last digit shown. ρ^*/ρ_s = Relative density, $\varepsilon_{el} = \frac{\Delta l}{l_0}$ (elastic strain), $W = \int_0^{\varepsilon_D} \sigma d\varepsilon$ (energy absorption per unit volume), $\sigma_P = \frac{1}{n} \cdot \sum_{i=1}^{n} \sigma_i$ (average value of the stress plateau), σ_I = Initiation stress, ε_I = Initiation strain, $\Delta\sigma_a = \sqrt{\frac{1}{N}\sum_{i=1}^{N}(\sigma_i - \sigma_P)^2}$ (amplitude of stress undulations (standard deviation of σ_P)), ε_D = Densification strain, $\Delta\varepsilon_P = \varepsilon_D - \varepsilon_I$ (plateau strain), E^* = Modulus of the honeycomb (slope of the linear elastic region).

l/t = 5	$Zr_{35}Ti_{30}Cu_{7.5}Be_{27.5}$	$Pt_{57.5}Cu_{14.7}Ni_{5.3}P_{22.5}$	2004Al	Zn	PEEK	PE
σ_I [MPa]	80.9	72.5	33.7	2.2	2.7	0.1
σ_p [MPa]	45.7	60.8	35.2	4.4	3.2	0.1
ε_D [%]	68.4	65.8	41.6	66.5	68.6	64.6
W [MPa]	31.0	38.6	15.0	2.8	2.0	6.0×10^{-2}
$\Delta\sigma_a$ [MPa]	19.4	15.7	4.3	1.9	0.7	1.0×10^{-2}
ε_{el} [%]	5.4	7.5	4.2	0.2	2.7	27.4
E^* [MPa]	1730.0	1840.0	1220.0	103.0	45.0	0.2
ρ [g/cm^3]	3.9	15.0	2.8	7.1	1.3	0.9

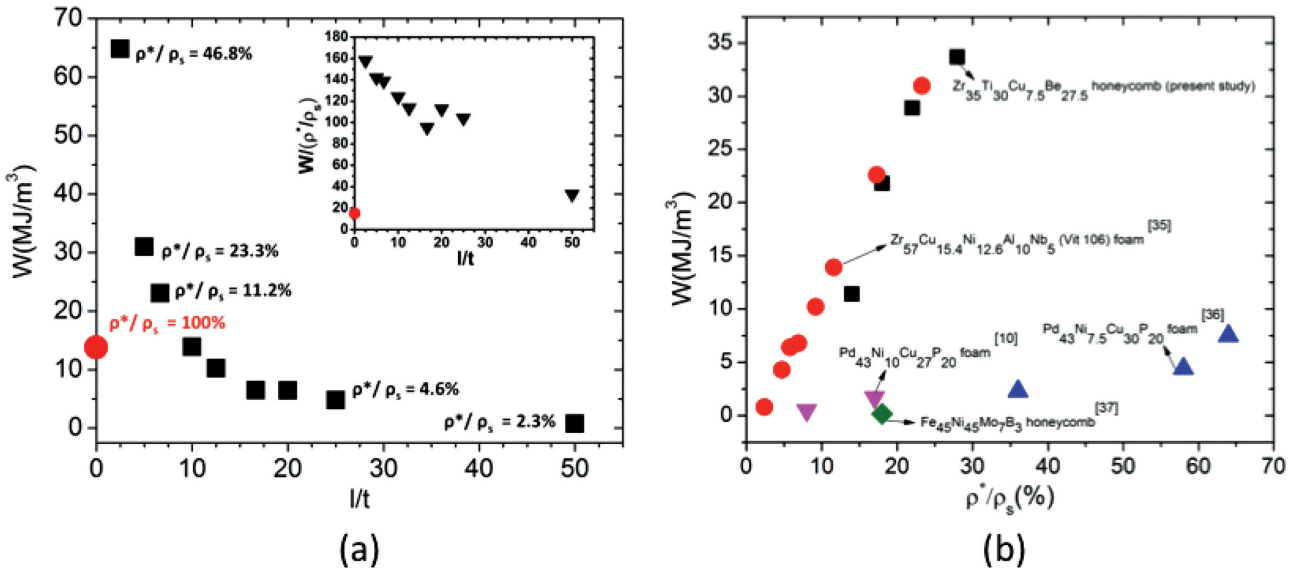

Figure 7. a) Energy absorption per unit volume ($W = \int_0^{\varepsilon_D} \sigma d\varepsilon$) for $Zr_{35}Ti_{30}Cu_{7.5}Be_{27.5}$ honeycombs with varying l/t ratio. Ligament length is constant at 500 μm. Energy absorption of the bulk sample is indicated by the red circle. ρ^*/ρ_s represents the relative density (ρ^*: honeycomb density, ρ_s: BMG's bulk density). The inset shows the energy absorption values normalized by the relative density of the honeycomb, where the normalized energy absorption ($W/(\rho^*/\rho_s)$) for $l/t = 50$ surpasses that of the bulk BMG sample. b) A comparison of energy absorption of BMG cellular structures including $Zr_{35}Ti_{30}Cu_{7.5}Be_{27.5}$ honeycomb (present study), $Zr_{57}Cu_{15.4}Ni_{12.6}Al_{10}Nb_5$ open-cell foam, $Pd_{43}Cu_{27}Ni_{10}P_{20}$ foam, and $Fe_{45}Ni_{45}Mo_7B_3$ honeycomb.

honeycomb, and considered fillets with radius ranging 1–50 μm (**Figure 8**a). Our results reveal a critical filleting radius of 6 μm above which the strength of the honeycomb doubles. Increasing this radius beyond 6 μm did not enhance the effect on initiation strength further. Our finding of such a critical ratio provides an effective design tool for increasing the strength of BMG honeycombs; strength doubled when corner-fillets are introduced at the expense of only 0.2% density increase.

For a honeycomb with $l/t > l/t_{crit}$, elastic buckling occurs. Because stresses are maximal at the honeycomb cell joints, yielding initiates at these regions. Microstructural analysis is carried out for $Zr_{35}Ti_{30}Cu_{7.5}Be_{27.5}$ honeycombs to reveal the fraction of the BMG honeycomb that plastically deforms, which indicates the effectiveness of the structure for energy absorbing applications (Figure 8b). Our findings reveal that deformation through shear banding occurs up to the densification limit (ε_D)

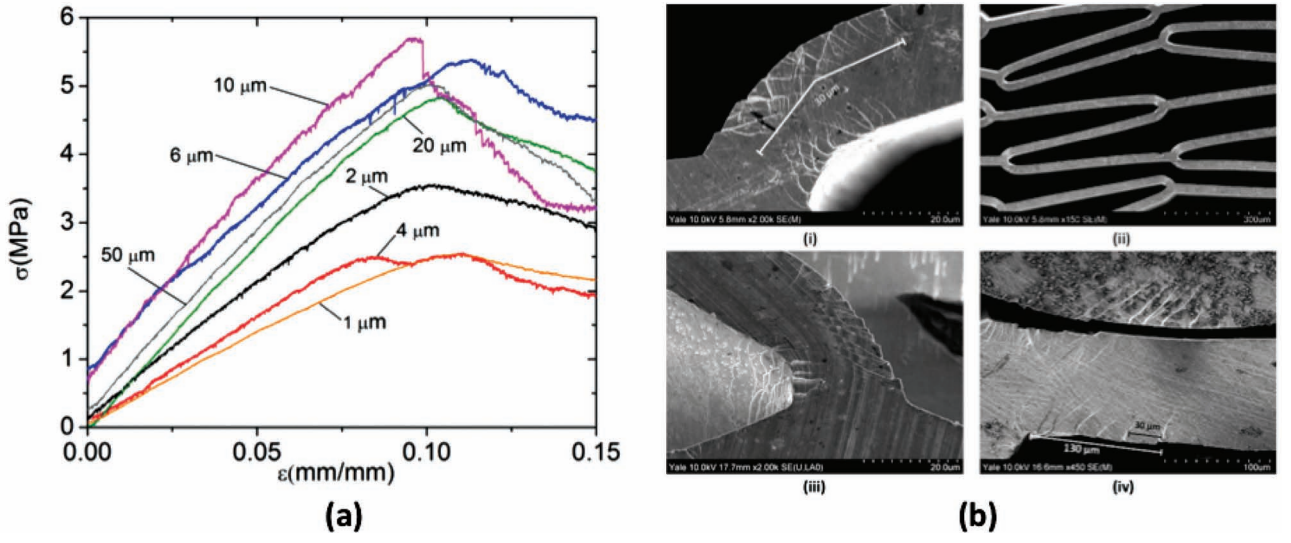

Figure 8. a) Effect of filleting corners of the honeycomb cell on the initiation strength of $Zr_{35}Ti_{30}Cu_{7.5}Be_{27.5}$ honeycomb ($l/t = 25$). Significant increase in σ_p is achieved for corner-fillet radius ≥6 μm. b) Corresponding SEM images of $Zr_{35}Ti_{30}Cu_{7.5}Be_{27.5}$ BMG honeycombs after deforming until ε_D. i,ii) Shear bands are localized at joints for corner-fillets with $r < 1$ μm ($l/t = 25$), and no shear band is observed at the ligaments. iii,iv) Shear bands are more homogenously distributed throughout the honeycomb when using corner-fillets with $r > 6$ μm with a shear band spacing of ~30 μm ((iii) $l/t = 25$ and (iv) $l/t = 10$), which spread out up to (iii) ~30 μm and (iv) ~130 μm.

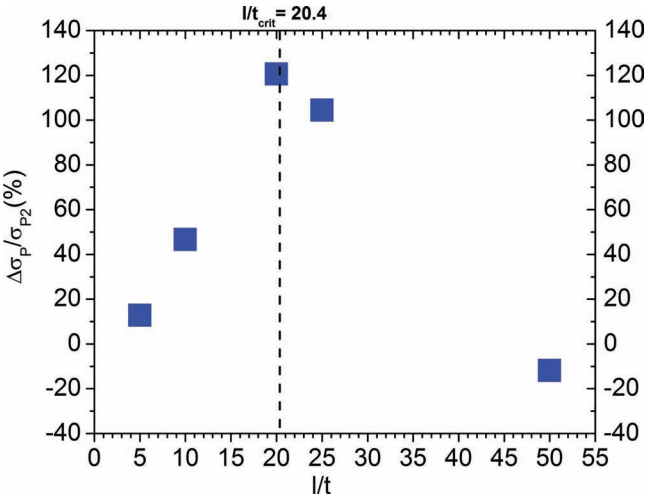

Figure 9. Effects of fillets on the plateau stress of Zr-BMG honeycombs as a function of l/t. Data points represent the difference of honeycombs with $r/t = 0.3$ and $r < 1$ μm. The effect of corner-fillets is most pronounced for $l/t \approx l/t_{crit}$. $\Delta\sigma_P$ is defined by the difference between the propagation strength of honeycombs with $r/t = 0.3$ (σ_{P2}) and $r < 1$ μm (σ_{P1}).

without an indication of fracture. The shear bands, which carry plastic deformation, are most densely present at the joints of the honeycombs. However, in honeycombs with corner-fillets, shear bands distributed more evenly throughout the honeycomb cell, hence utilizing a larger fraction of the honeycomb cell, which results in higher energy absorption (Figure 8b (iii) and (iv)).

To identify geometries where corner-fillets are most effective for $Zr_{35}Ti_{30}Cu_{7.5}Be_{27.5}$ honeycombs, we compared the effects of filleting for various l/t ratios. As a measure, two kinds of corner-fillet geometries were considered, $r/t = 0.3$ (6 μm for $l/t = 20$) and $r/t < 1$ μm (smallest radius possible with the resolution of photolithography) (**Figure 9**). The effect of filleting on σ_P is most pronounced for $l/t \cong l/t_{crit}$.

The properties of BMG forming alloys can be dramatically altered by annealing, which results in structural relaxation or crystallization.[38–43] To explore the effect of BMG properties on the performance of the honeycombs, we annealed the Zr-BMG honeycombs at temperatures below and above the glass transition temperature for comparable times with structural relaxation and crystallization. Sub-T_g embrittlement is achieved by annealing the as-formed honeycomb at 275 °C for 18 h, whereas the crystallized honeycomb is formed by heating to 400 °C (above-T_g) for 30 min.[43] Their performances are compared to the as-formed honeycomb of the same l/t ratio (**Figure 10**). The embrittled and crystallized honeycombs show pronounced shear localization and a yield plane close to 45° to the applied load where cell walls fracture (Figure 10b). The as-formed honeycomb, on the other hand, deforms through row collapsing parallel to the applied stress achieved by plastic deformation of the ligaments without fracture. Initiation, propagation strength, and elastic strain limit of the embrittled and crystallized honeycombs are lower than those of the amorphous honeycomb. These findings, together with the comparison of BMG honeycomb with honeycombs made of different materials, demonstrate the importance of the materials property for the honeycomb's performance (**Table 2**).

3. Conclusions

Here, we introduce an effective method that combines lithography and thermoplastic forming to fabricate test microstructural architectures from bulk metallic glasses at high precision. We used this highly versatile technique to explore bulk metallic glasses in honeycomb structures.

BMG honeycombs absorb large amounts of energy, up to five times more than in bulk form, because in the honeycomb structure a size effect is utilized, which promotes plastic deformation. The deformation made of a BMG honeycomb can be altered from brittle to ductile through varying the ratio of ligament length to ligament thickness. Furthermore, we identified cell corner-fillets as effective design features; a 0.2% increase in density doubles strength and energy absorption.

More generally, our approach to fabricate, characterize, and optimize the architectural design of a honeycomb for bulk metallic glasses can be used to investigate a wide range of stochastic and periodic microstructural architectures, particularly those where current fabrication and characterization methods are challenged.

4. Experimental Section

Si Mold Fabrication: BMG honeycomb molds were designed using AutoCAD 2008 software program. The drawing layout was transferred to a photomask maker (Heidelberg DWL-66 Laser Mask Writer) through direct laser beam writing. A thin layer of photoresist (8-μm AZ P4620 coating) on Si wafer was patterned by UV exposure through the photomask. The etching depth of the honeycomb molds was measured to be around 300 ± 30 μm. The etch cycle for DRIE processing was carried out under 12 s, 130-sccm SF_6, 13-sccm O_2, 600-W coil power, 12-W platen power, and 26-mtorr pressure, whereas the passivation cycle was carried out under 8 s, 85-sccm C_4F_8, 600-W coil power, 0-W platen power, and 15-mtorr pressure. Residual resist was subsequently cleaned from the surface by soaking first in acetone, then in isopropanol, and finally in deionized water. The Si wafer was finally dried with N_2 under a pressure of 2×10^5 Pa.

BMG Alloy Production: $Zr_{35}Ti_{30}Cu_{7.5}Be_{27.5}$ BMG former was prepared by melting the constituents with purity higher than 99.99% in an arc melter. In order to prepare amorphous samples, the cast ingot was sealed in a quartz tube under vacuum, heated above its liquidus temperature for 5 min, and quenched in water respectively. $Pt_{57.5}Cu_{14.7}Ni_{5.3}P_{22.5}$ was prepared by melting the elements of purity better than 99.99% in a vacuum-sealed quartz tube. B_2O_3 was used to flux the ingot for 15 min, which was shown to increase the glass forming ability by reducing the alloy's oxides. An amorphous rod was obtained by casting it in a quartz tube, and by subsequent water quenching. X-ray diffraction machine (XRD-6000 Shimadzu) and differential scanning calorimeter (Perkin Elmer Diamond DSC) confirmed that both BMG formers are fully amorphous.

BMG Honeycomb Fabrication: BMG discs cut from the amorphous samples were pre-pressed to a thickness of around 500 μm by using Instron 5569 tensile testing machine (50 kN maximum load capacity) with the compression compartments. BMG honeycombs were fabricated by thermoplastic forming (TPF) of $Zr_{35}Ti_{30}Cu_{7.5}Be_{27.5}$ BMG former at 425 °C (275 °C for $Pt_{57.5}Cu_{14.7}Ni_{5.3}P_{22.5}$) into the honeycomb mold for 60 s under a pressure of 50 MPa by using the same setup. Uniform heating was provided by the heating cartridges embedded to these fixtures. The extra BMG layer was removed by grinding and polishing using Buehler Metaserv 250 Grinder-Polisher. The aspect-ratio dependent etching rate of Si molds result in honeycombs varying in depth. Samples are grinded down to 200 ± 10 μm to have uniformity in starting depth of the BMG honeycombs with different l/t ratio. BMG honeycomb released from the mold by etching the Si mold in KOH solution for 30 min at 100 °C.

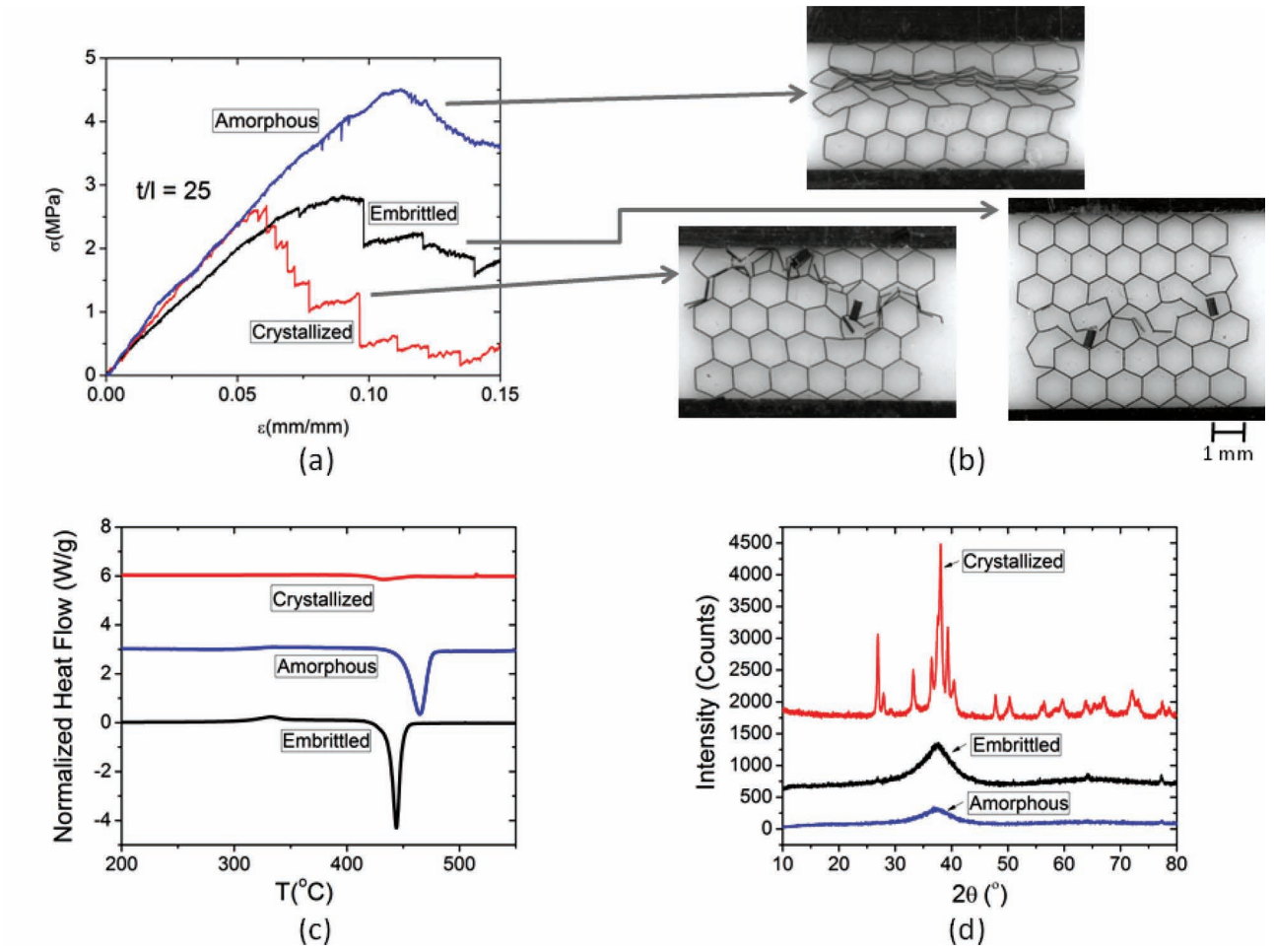

Figure 10. Influence of sub-T_g (embrittlement) and above-T_g (crystallization) annealing on mechanical properties of Zr-BMG honeycombs ($l/t = 25$ constant). a) Mechanical properties and b) deformation behavior of as-formed, embrittled, and crystallized honeycombs are compared. c) Normalized heat flow and d) XRD spectrum of the differently processed honeycombs.

The amorphous structure was subsequently checked by DSC and XRD measurements.

Mechanical Characterization of BMG Honeycombs: Quasi-static compression of in-plane compression of honeycombs was conducted by using Instron 5543 tensile testing machine (1 kN maximum load capacity). To increase the accuracy, various load cells were used (10 N, 100 N and 1000 N) depending on the l/t ratio of the honeycomb. Custom made pneumatic grips with grids were utilized to prevent

Table 2. Mechanical Properties of BMG honeycombs for different l/t ratios. Errors are on the order of the last digit shown. ρ^*/ρ_s = Relative density, $E^*_{theo} = 2.3\,E_s\left(\frac{t}{l}\right)^3$ (calculated theoretical modulus of the honeycomb), $\sigma_{l\_theo} = \frac{2}{3}\sigma_\gamma\left(\frac{t}{l}\right)^2$ (calculated theoretical initiation strength of the honeycomb). 20_cryst: crystallized sample ($l/t = 20$), 20_emb: embrittled sample ($l/t = 20$).

l/t	50	25	20	16.7	12.5	10	6.7	5	2.5	20_cryst	20_emb	Bulk[25]
ρ^*/ρ_s [%]	2.4	4.7	5.8	6.9	9.2	11.6	17.3	23.3	46.8	4.7	4.7	100.0
ε_{el} [%]	24.0	11.4	10.4	7.8	6.7	6.5	6.2	5.4	5.2	1.0E-02	0.1	2
W [MPa]	0.8	4.3	6.4	6.8	10.2	13.9	22.6	31.0	64.8	1.2	1.8	14.3
σ_p [MPa]	0.9	5.2	8.4	8.6	13	18.8	31.2	45.7	108.3	1.48	2.36	-
σ_l [MPa]	1.0	5.4	7	10.1	12.2	22.3	49.2	80.9	301.2	2.7	2.8	1430.0
$\sigma_{l\ theo}$ [MPa]	0.2	1.3	2.5	3.5	6.3	9.8	22.1	39.2	-	1.3	1.3	-
$\Delta\sigma a$ [MPa]	0.2	1.0	1.3	1.4	3.1	5.1	10.5	19.4	46.0	0.7	0.3	-
ε_D [%]	85.4	84.2	78.3	81.4	81.7	75.8	72.2	68.4	64.8	82.3	77.1	-
E^* [MPa]	8.9	46	61	130	215	365	920	1730	5600	46	38	-
E^*_{theo} [MPa]	1.6	12.8	25	43.2	102.3	199.9	674.6	1599	-	12.8	12.8	86900

slippage and guarantee precise alignment. The steel mold consists two steel pieces for the top tensile grip, and a steel piece and a transparent glass panel for the bottom grip. Top and bottom parts, which are individually screwed to each other, include flat steel plates standing in between. The honeycomb was resting on the bottom plate, which was positioned between the metal mold and the transparent glass panel with a clearance exceeding the depth of the honeycomb. Alumina piece was placed under the base plate to increase the contrast of the honeycomb during imaging. Using Instron Bluehill Software, in-plane compression of the honeycomb was achieved by pressing the top plate with a controlled strain rate of 0.005 mm/s in air. In-situ recording through the transparent glass panel while the deformation of the honeycomb was carried out by Keyence Digital Microscope VHX-500F, by which the images were simultaneously recorded. SEM imaging (Model: Hitachi SU-70) was subsequently conducted to determine the distribution and spacing of the shear bands.

Heat Treatment of BMG Honeycombs: As-formed $Zr_{35}Ti_{30}Cu_{7.5}Be_{27.5}$ BMGs was exposed to 275 °C for 18 h for sub-T_g embrittlement, whereas the crystallized honeycomb was achieved by heating to 400 °C (above-T_g) for 30 min using Vulcan Box Furnace (Model No: 3-550). In-plane compression test was carried out by using the same setup described in mechanical characterization of BMG honeycombs. DSC and XRD measurements were conducted to understand effect of heat treatment over mechanical characterization.

Supporting Information

Supporting Information is available from the Wiley Online Library or from the author.

Acknowledgements

This work was supported by the Department of Energy through the Office of Basic Energy Sciences (#DE SC0004889), and DARPA through the MCMA program (W911NF-11-1-0380). The authors thank A. J. Barnes and Superform USA for providing 2004Al superplastic aluminum alloy and Michael Kanik for helping with the stage setup.

Received: February 24, 2012
Published online: April 23, 2012

[1] A. L. Greer, *Mater. Today* **2009**, *12*, 14.
[2] F. Spaepen, *Acta Metall.* **1977**, *25*, 407.
[3] R. D. Conner, W. L. Johnson, N. E. Paton, W. D. Nix, *J. Appl. Phys.* **2003**, *94*, 904.
[4] J. Schroers, C. Veazey, W. L. Johnson, *Appl. Phys. Lett.* **2003**, *82*, 370.
[5] A. H. Brothers, D. C. Dunand, *Appl. Phys. Lett.* **2004**, *84*, 1108.
[6] J. Schroers, C. Veazey, M. D. Demetriou, W. L. Johnson, *J. Appl. Phys.* **2004**, *96*, 7723.
[7] A. H. Brothers, D. C. Dunand, *Adv. Mater.* **2005**, *17*, 484.
[8] T. Wada, A. Inoue, A. L. Greer, *Appl. Phys. Lett.* **2005**, *86*, 251907.
[9] A. H. Brothers, D. C. Dunand, Q. Zheng, J. Xu, *J. Appl. Phys.* **2007**, *102*, 023508–1.
[10] M. D. Demetriou, C. Veazey, J. S. Harmon, J. P. Schramm, W. L. Johnson, *Phys. Rev. Lett.* **2008**, *101*, 145702.
[11] A. G. Evans, J. W. Hutchinson, N. A. Fleck, M. F. Ashby, H. N. G. Wadley, *Prog. Mater. Sci.* **2001**, *46*, 309.
[12] B. A. Bouwhuis, G. D. Hibbard, *Mater. Sci. Eng. A* **2010**, *527*, 565.
[13] N. T. Kirkland, I. Kolbeinsson, T. Woodfield, G. Dias, M. P. Staiger, *Int. J. Mod. Phys. B* **2009**, *23*, 1002.
[14] J. Schroers, Q. Pham, A. Desai, *J. Microelectromech. Sys.* **2007**, *16*, 240.
[15] J. Schroers, *Adv. Mater.* **2010**, *22*, 1566.
[16] B. Sarac, G. Kumar, T. Hodges, S. Y. Ding, A. Desai, J. Schroers, *J. Microelectromech. Sys.* **2011**, *20*, 28.
[17] J. Schroers, T. M. Hodges, G. Kumar, H. Raman, A. J. Barnes, P. Quoc, T. A. Waniuk, *Mater. Today* **2011**, *14*, 14.
[18] L. J. Gibson, M. F. Ashby, G. S. Schajer, C. I. Robertson, *Proc. R. Soc. London Ser. A* **1982**, *382*, 25.
[19] M. F. Ashby, *Metall. Trans. A* **1983**, *14*, 1755.
[20] S. D. Papka, S. Kyriakides, *J. Mech. Phys. Solids* **1994**, *42*, 1499.
[21] N. A. Fleck, C. Chen, T. J. Lu, *J. Mech. Phys. Solids* **1999**, *47*, 2235.
[22] Y. Saotome, K. Imai, S. Shioda, S. Shimizu, T. Zhang, A. Inoue, *Intermetallics* **2002**, *10*, 1241.
[23] D. L. Henann, V. Srivastava, H. K. Taylor, M. R. Hale, D. E. Hardt, L. Anand, *J. Micromech. Microeng.* **2009**, *19*, 1.
[24] K. Takenaka, N. Saidoh, N. Nishiyama, A. Inoue, *Nanotechnology* **2011**, *22*, 105302.
[25] G. Duan, A. Wiest, M. L. Lind, J. Li, W. K. Rhim, W. L. Johnson, *Adv. Mater.* **2007**, *19*, 4272.
[26] J. Schroers, W. L. Johnson, *Phys. Rev. Lett.* **2004**, *93*, 255506–1.
[27] J. Schroers, *Acta Mater.* **2008**, *56*, 471.
[28] G. Kumar, H. X. Tang, J. Schroers, *Nature* **2009**, *457*, 868.
[29] K. Ohsaka, S. K. Chung, W. K. Rhim, A. Peker, D. Scruggs, W. L. Johnson, *Appl. Phys. Lett.* **1997**, *70*, 726.
[30] L. J. Gibson, M. F. Ashby, *Cellular Solids - Structure and Properties*, Second ed., (Eds: D. R. Clarke, S. Suresh, I. M. Ward FRS) Cambridge University Press, Cambridge UK **2001**, p. 113.
[31] Superplastic Aluminum Alloys: KEY to METALS Article, http://www.keytometals.com/page.aspx?ID=CheckArticle&site=ktn&NM=264 (accessed April 2012).
[32] Mechanical and Physical Properties of Materials | Matbase - Material Properties Database, http://www.matbase.com/, (accessed April 2012).
[33] M. M. Trexler, N. N. Thadhani, *Prog. Mater. Sci.* **2010**, *55*, 759.
[34] Z. F. Zhang, J. Eckert, L. Schultz, *Acta Mater.* **2003**, *51*, 1167.
[35] A. H. Brothers, D. C. Dunand, *Acta Mater.* **2005**, *53*, 4427.
[36] M. D. Demetriou, J. C. Hanan, C. Veazey, M. Di Michiel, N. Lenoir, E. Ustundag, W. L. Johnson, *Adv. Mater.* **2007**, *19*, 1957.
[37] J. C. Hanan, B. Jayakumar, A. Bhat, *Imece2009: Proc. Asme Int. Mech. Eng. Congress and Exposition,* Vol *2* **2010**, 73.
[38] C. J. Gilbert, R. O. Ritchie, W. L. Johnson, *Appl. Phys. Lett.* **1997**, *71*, 476.
[39] C. Nagel, K. Ratzke, E. Schmidtke, F. Faupel, *Phys. Rev. B* **1999**, *60*, 9212.
[40] A. Slipenyuk, J. Eckert, *Scripta Mater.* **2004**, *50*, 39.
[41] B. P. Kanungo, S. C. Glade, P. Asoka-Kumar, K. M. Flores, *Intermetallics* **2004**, *12*, 1073.
[42] P. Murah, U. Ramamurty, *Acta Mater.* **2005**, *53*, 1467.
[43] G. Kumar, D. Rector, R. D. Conner, J. Schroers, *Acta Mater.* **2009**, *57*, 3572.